

# Adaptive optics system for the new Swedish solar telescope

Göran B. Scharmer<sup>a</sup>, Peter Dettori<sup>a</sup>, Mats G. Löfdahl<sup>a</sup>, Mark Shand<sup>b</sup>

<sup>a</sup>Institute for Solar Physics of the Royal Swedish Academy of Sciences

<sup>b</sup>Systems Research Center, Hewlett-Packard Laboratories

## ABSTRACT

The 1-meter Swedish solar telescope is a new solar telescope that was put in operation on the island of La Palma in the Canary Islands at the end of May 2002. The goal of this telescope is to reach its diffraction limited resolution of 0.1 arcsec in blue light. This has already been achieved by use of a low-order adaptive optics (AO) system. This paper describes the AO system initially developed for the former 50-cm Swedish Vacuum Solar Telescope (SVST) and further improved for the new telescope. Both systems use a combination of bimorph modal mirrors and Shack–Hartmann wavefront sensors. Unique to these systems are that they rely on a single workstation or a PC to do all the computations required to extract and pre-process the images, measure their positions using cross correlation techniques and for controlling the deformable mirror. This is in the present system possible by using the `FERR` instruction available on Compaq's Alpha architecture and in the new system using the `PSADDBW` instruction, available on Pentium 4 and Athlon processors. We describe both these systems with an emphasis on the performance, the ease of support and upgrades of performance.

We also describe the optimization of the electrode geometry for the new 37-electrode bimorph mirror, supplied by AOPTIX Technologies, Inc.,<sup>1</sup> for controlling Karhunen–Loève modes. Expected performance, based on closed-loop simulations, is discussed.

**Keywords:** Telescopes, optics, wavefront sensing, adaptive optics

## 1. INTRODUCTION

The 1-meter Swedish solar telescope<sup>2,3</sup> is designed to be the highest resolving solar telescope in the world at the time of deployment. In particular, its goal is to reach its diffraction limited resolution of 0.1 arcsec at 430 nm, a wavelength of particular importance for viewing bright points associated with magnetic field. Achieving this resolution over extensive periods of time requires excellent seeing and an adaptive optics (AO) system with at least 30 electrodes. Such an AO system of relatively low order will give smaller residual wavefront error on a 1-meter solar telescope than was the case for the previous 50-cm solar telescope without adaptive optics.

In this paper we describe the AO system developed for the new solar telescope, which is intended for use in very good seeing. It is designed to be a low-cost system that is simple to develop, maintain, calibrate and use. Section two describes the re-imaging system including the tip-tilt system, the science CCDs, and the present AO system. Section three describes the new 37-electrode bimorph mirror and the method used to optimize the electrode geometry with respect to correction of Karhunen–Loève (KL) modes and the wavefront sensor.

## 2. DESCRIPTION OF THE CURRENT AO SYSTEM

### 2.1. Optical setup

The 1-meter Swedish solar telescope has an optical system consisting of a 1.1-meter fused silica singlet lens with a clear aperture of 97 cm, two 1.4-meter optical flats and a 60 mm field mirror re-imaging the entrance pupil on a Schupmann corrector, consisting of a 305 mm fused silica lens and a 300 mm Zerodur mirror.<sup>2,3</sup> This optical system is in vacuum, with the 1.1-meter lens acting as vacuum window. Eight mm inside the focal plane of the Schupmann system is located a 50 mm field lens that also serves as exit vacuum window. The combined AO and re-imaging system is located outside the vacuum system on the optical table and includes a tip-tilt mirror with CCD used to measure the position of solar fine structure, the wavefront sensor and the science CCDs, see Fig. 1.

---

Further author information: G.B.S.: E-mail: [scharmer@astro.su.se](mailto:scharmer@astro.su.se), WWW: [www.solarphysics.kva.se/](http://www.solarphysics.kva.se/), Postal address: Institute for Solar Physics, AlbaNova University Center, SE-106 91 Stockholm, Sweden

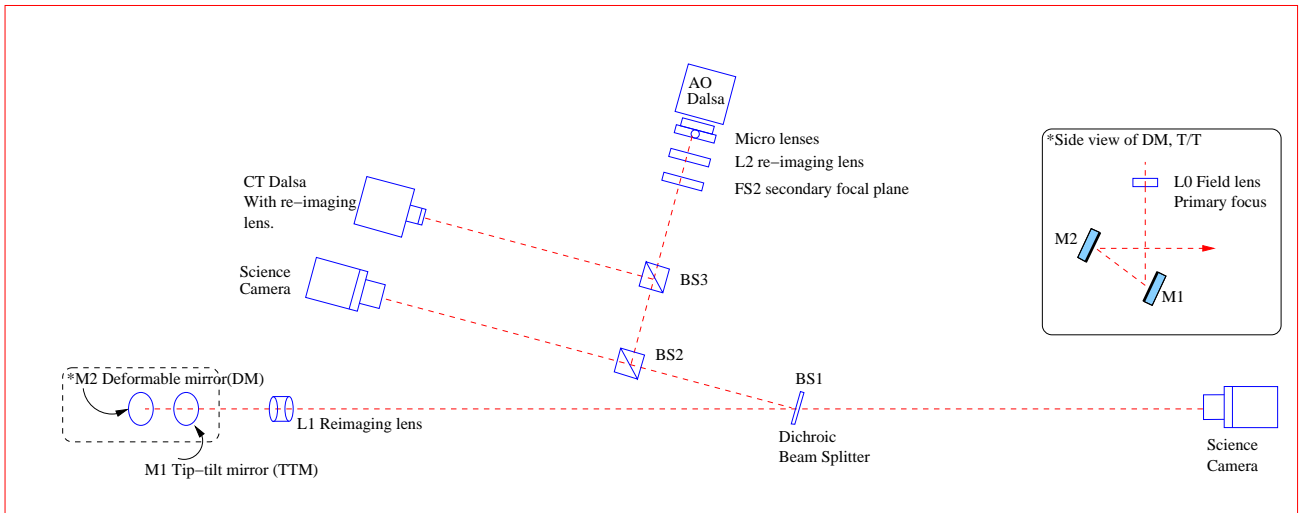


**Figure 1.** The schematic drawing shows the layout of the optics on the optical table. The beam from the telescope is nearly vertical and is reflected first off the tip-tilt mirror and then off the adaptive mirror through the re-imaging lens (L1). Shown are also the locations of the beam splitters, two science CCD:s, the AO wavefront sensor and the correlation tracker CCD used to control the tip-tilt mirror.

The distance between the field lens and adaptive mirror, matched by the focal length of the field lens, determines the pupil diameter. During design of the system, it was decided that the optimum pupil diameter for the adaptive mirror was around 34 mm. A small pupil diameter leads to high resonance frequency of the adaptive mirror, makes the overall system compact, reduces internal seeing effects and the dimensions of the optical components which also helps improve optical quality. The manufacturer of the bimorph mirror, AOPTIX Technologies Inc.,<sup>1</sup> concluded that a 34 mm pupil diameter would allow correction of up to 60 KL modes which is considered the upper limit for future developments of this AO system.

Following the Schupmann focus is first the tip-tilt mirror, then the adaptive mirror and the re-imaging lens, where the pupil image is on the adaptive mirror. The reason for having the tip-tilt mirror first is that the diameter of the Schupmann focal plane is smaller than the pupil diameter so the beam diameter increases from the Schupmann focal plane to the re-imaging lens and this allows a smaller tip-tilt mirror than if it were placed behind the adaptive mirror. The re-imaging lens is located after the adaptive mirror to allow changes of the image scale without affecting the tip-tilt and adaptive mirrors. It is to be noted, though, that changes of the re-imaging lens requires changes of the wavefront sensor optics. The present re-imaging lens is a 55 mm diameter cemented apochromatic triplet which, because of its short focal length, provides a nearly perfectly flat focal curve throughout the visible part of the spectrum.

The tip-tilt and adaptive mirrors fold the beam from nearly vertical to horizontal, or approximately by 90°. This is arranged such that the tip-tilt mirror deflects the beam 60° and the adaptive mirror by 30°. With an angle of incidence of 15° on the adaptive mirror, the pupil image is nearly circular (since  $\cos 15^\circ = 0.97$ ). The re-imaging lens magnifies the image by approximately 2.2 times, producing an image scale of 0.041 arcsec per pixel on our Eastman Kodak Megaplug 1.6 and 4.2 science CCDs.

The tip-tilt and adaptive mirrors plus the re-imaging lens will be mounted on a rotating stage that allows the beam to be deflected to either a combined spectrograph and spectro-polarimeter or to an optical table intended for re-imaging through broad-band and narrow-band filters. For re-imaging, the following beam includes a dichroic beam splitter and several beam splitter cubes to divide the light among up to four science CCDs, the wavefront sensor and the correlation tracker CCD. The beam splitter diverting light to the wavefront sensor is close to the final focal plane of the beam reflected by the dichroic.

The Schupmann focus, located before the adaptive mirror, is used for obtaining a control matrix for the adaptive mirror and for co-aligning and co-focusing the science CCDs.

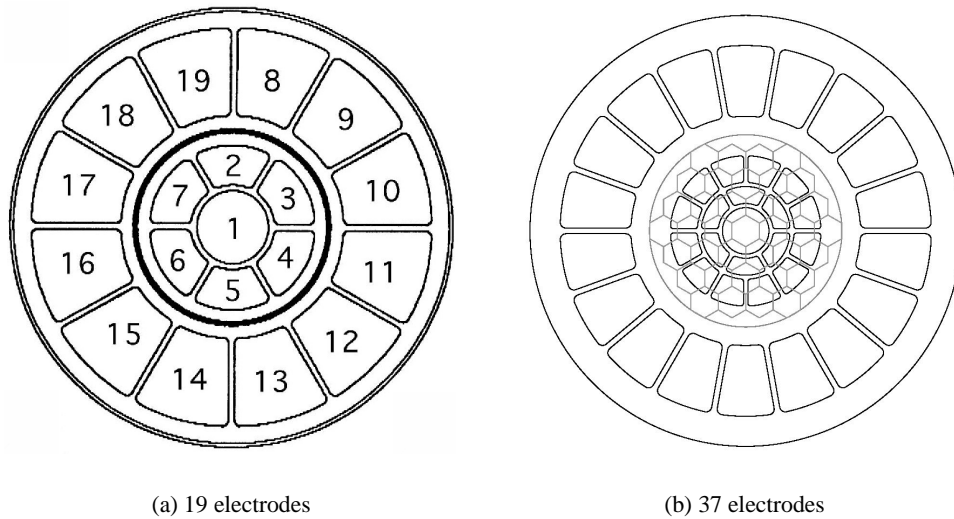


**Figure 2.** The figure compares the geometries of the old 19-electrode (a) and the new 37-electrode (b) bimorph mirrors, to the same scale. Figure (b) also shows the 37-element hexagonal micro-lens array superimposed in grey. The pupil diameter is the same for the two mirrors and indicated by the thick circle in (a) and a grey circle in (b).

## 2.2. Deformable mirror

The optimum modes for compensating atmospheric seeing are KL modes in the sense that the smallest possible residual wavefront error can be achieved with a given number of corrected modes.<sup>4</sup> For example, perfect correction of the 30 first KL modes is equivalent to approximately 50 corrected modes for a mirror providing zonal correction.<sup>4</sup> Low-order KL modes have the advantage of being similar to pure focus, coma, astigmatism and spherical aberration which are likely to appear in solar telescopes from misalignment of the optics, imperfections in the mirror cells and temperature gradients in the transmitting optics, such as vacuum windows (if present), and re-imaging lenses. Designing the deformable mirror to compensate Zernike or KL modes, allows good correction also of such fixed or slowly varying telescope aberrations.

Bimorph mirrors have the attractive property that they easily produce low-order aberrations with large amplitude and that higher-order aberrations are produced with lower amplitude. This makes them ideally suited for compensating seeing from atmospheric turbulence and very likely also for compensating telescope aberrations as well as wavefront errors from polishing. Bimorphs produce small amounts of high-order mirror modes and therefore also small amounts of aliasing from high to low-order modes in the wavefront sensor.

The present 19-electrode deformable mirror was designed by AOPTIX for correcting approximately the first 15 Zernike modes. The second mirror, which is presently in the process of being delivered, was designed by the authors to correct approximately the first 30 KL modes (see Section 3.2 for details). Figure 2 shows the geometries of the present 19-electrode mirror and that of the new 37-electrode mirror with the 37 micro-lenses superimposed in grey. The geometry of the 37-electrode mirror was obtained from optimizations described in Section 3. Note the good match between the electrode and micro-lens geometries.

## 2.3. Wavefront Sensor

The wavefront sensor is of Shack–Hartmann type and built from commercially available components in order to reduce cost.

The potentially most expensive part of the wavefront sensor is the CCD. Based on analysis of open-loop wavefront sensor data, it was decided that a frame-rate of 1 kHz would be adequate. Closed-loop performance on the SVST verified this in normal operation but also demonstrated the need for improved bandwidth in higher wind speed. This improvement was later obtained by rewriting the code in order to reduce time-delay (see Section 2.7).

Of the commercially available CCDs, we chose the Dalstar CA-D6, which provides 955 fr/sec. This CCD has  $260 \times 260$  pixels which are read out in 4 separate  $65 \times 260$  pixel channels. The image size is a little larger than required. By ensuring that the micro-lens images are re-imaged on the part of the CCD which is first read out it is possible to process sub-images on the fly as they are written to memory.

In order to provide a good match to the Zernike or KL modes of the bimorph mirror, the nearly circular arrangement of hexagonal micro lenses is superior to that of square micro lenses. Simulations have shown, as expected, that a modified hexagonal geometry where the outermost ring of micro lenses is displaced to the perimeter of the pupil, would give the best performance, but the cost of such a solution was too high and standard micro lenses from Adaptive Optix Associates Inc.<sup>5</sup> were chosen.

The wavefront sensor optics was designed and verified with Zemax. The constraints were the F-ratio of the re-imaging optics, the pixel size of the CCD ( $10 \mu\text{m}$ ) and the desired image scale at the focal plane of the CCD. A satisfactory solution was found based on available lenses and micro lenses. The optics consists of a field lens, a second lens to compensate mismatch in the focal length of the field lens and an  $f = 40 \text{ mm}$ ,  $0.625 \text{ mm}$  period micro-lens array. The design allows the same micro-lens array to be used for either re-imaging five (for the 19-electrode mirror) or seven (for the 37-electrode mirror) micro lenses across the pupil diameter. The field lens is different for the two designs as are the positions of the two lenses. The micro lens array can be at a fixed position relative to the CCD. The image scale on the CCD is  $0.3 \text{ arcsec/pixel}$  for the 19 micro lens and  $0.43 \text{ arcsec/pixel}$  for the 37 micro lens setups.

#### **2.4. Control matrix and wavefront calibration**

A good match between the deformable mirror and the wavefront sensor allows straightforward and accurate calibration procedures.

To measure the control matrix, a large pinhole for use with solar light or a small pinhole for use with a laser is inserted at the primary focus, before the deformable mirror. With the present mirror, for each of the 19 electrodes, a low-frequency sawtooth wave of relatively large amplitude is output during approximately 1 s while the AO software determines all Zernikes 2–19, for each frame. This step of the calibration takes a total of 20 s and results in 19,000 wavefront measurements which are stored on disk. When the data has been stored, an off-line reduction program written in ANA<sup>6</sup> (an IDL-like but non-commercial language) processes the data. The processing consists of using least-squares fits to determine the best linear relation between input voltage and output Zernikes for each of the 19 electrodes. By using 1000 measurements, low-noise measurements are achieved which are limited in practice by any small seeing changes within the AO setup during 1 second. This processing takes approximately 10 s, by taking advantage of the high speed of the same workstation as used to control the AO system.

We also consider it important to be able to calibrate the zero-point wavefront (“flatten the mirror”) without having to rely on external wavefront sensors or theoretical calculations of the electrode response. Our experience with the 19-electrode suggests that the mirror can be flattened to between  $\lambda/40$  and  $\lambda/30$  RMS by using only a pinhole near the wavefront sensor focus as reference.

#### **2.5. AO computer**

Whereas the implementation of early night-time AO systems required the use of DSPs to handle the tasks of processing micro-lens images, performing matrix multiplications and outputting voltages to the deformable mirror, we recognized that DSPs have a number of disadvantages and that general purpose microprocessors had developed to the point where a single such processor may be able to do all the processing required even for an AO system relying on cross-correlations to measure the positions of the sub-images. A comparison between DSPs and general purpose processors is discussed at depth in Refs. 7, 8 and will not be repeated here. It suffices to summarize this discussion as follows.

Advances in computer architecture such as caches and superscalar pipelined execution units have rendered general purpose microprocessors as efficient per clock tick as DSPs.<sup>9</sup> At the same time the clock speed of general purpose microprocessors have out-paced DSPs such that the uniprocessor performance of modern general purpose microprocessor greatly exceeds that of current DSPs. While a number of DSPs can be combined to mitigate the advantages of the general purpose microprocessor, such combining entails communication overheads and complicates algorithms.

To maximize performance, DSPs tend to expose the internal architecture of the processor to a much greater extent than does a general purpose microprocessor. As a consequence, it is difficult to write efficient compilers of languages

**Table 1.** CPU time spent on various tasks in the AO code in  $\mu s$ , given for use on extended targets (cross-correlations) on Alpha and Athlon platforms. Timing is for 19 sub-images, 18 Zernikes and a 19-electrode bimorph mirror. Each sub-image has  $16 \times 16$  pixels except the reference sub-image ( $24 \times 24$  pixels). Cross-correlations are done by evaluating all possible  $\pm 4$  pixel shifts.

Task	Alpha 566MHz	Athlon 1400MHz
Unpacking DALSA 16 bit data	79	122
Flat-field, dark corr, max, min, average intensities	119	46
Sub-image position estimate, cross-correlation	200	220
Position to Zernike matrix multiply	0.2	0.4
Zernike to voltage matrix multiply	9	2
Miscellaneous	25	32
Total time	435	422

like C to DSPs and so they are often programmed in assembly language. Furthermore, there is limited compatibility in program code of successive generations of DSPs due to the internal architecture changes that accompany new generations. General purpose microprocessors on the other hand are careful to maintain compatibility between successive generations at the binary machine code level and between different architectural families through the provision of high-level language optimizing compilers which allow efficient applications to be written in a highly portable manner.

Crucial to an AO system for a solar telescope, is the ability to do cross-correlations extremely fast. Both the AO system and the correlation relies on the sum of absolute differences algorithm to yield a correlation function the minimum of which is obtained by quadratic interpolation. Without the availability of multimedia extensions in the form of dedicated instructions to perform parallel manipulation of multiple integer data items, such an AO system would be much more difficult to develop than was the case. In the present system, we are using the pixel error instruction (PERR), available on HP's (formerly DEC) Alpha platforms. This instruction computes the sum of absolute differences of eight pixels presented in two 64-bit input operands on a full eight bits per pixel and can be issued at the rate of one per machine cycle for the full sum of absolute differences calculation over 8 pixels in current Alpha implementations. At 566 MHz clock frequency, this implies that up to  $4.5 \times 10^9$  absolute differences can be evaluated per second. For the current system with 19 micro-lenses, the cross-correlations could in principle be carried out within 100  $\mu s$ , in practice about 200  $\mu s$  are required with the present code and clock frequency and data cache related stalls. Reducing the number of shifts from  $\pm 4$  to  $\pm 3$  after closing the servo-loop would reduce this time from 200  $\mu s$  to 120  $\mu s$ .

When developing the present system, it was expected that the Alpha workstations would soon be available with 1 GHz clock frequency. But Compaq have announced that they will be phasing out work on the Alpha processor in favor of the new Itanium 64 bit processor. Migrating to Itanium is a viable option since Itanium has a similar sum of differences instruction (PSAD1). We have however, already ported our code to the Pentium and Athlon platforms to investigate whether these platform are also viable. The Pentium 4 architecture implements 8 bit sum of difference instruction (PSADBW) that can operate on either 8 (64 bit) or 16 (128 bit) 8 bit pixels in one instruction. The AMD Athlon processor implements the 64 bit variant only, but our experience has shown that the Athlon processor can achieve similar performance with 8 pixels per instruction that the Pentium 4 achieves with 16 pixels per instruction. The sub-image position estimate in Table 1 compares the time spent in the optimized code on Athlon and Alpha processors.

## 2.6. Computational performance

Table 1 summarizes the CPU time spent on various tasks in the AO code. As can be seen in this table, only half of the computing time is spent on cross-correlations. The remainder of the time is dominated by the time needed to unpack the DALSA 16 bit words (2 pixels per word) as well as performing flat-field and dark corrections. This timing also includes an evaluation of the minimum, maximum and average intensities for each sub-image. These values are used in a rather elaborate scheme which aims at monitoring illumination changes for the different sub-images and continually adjusting the DC levels of the sub-images such that they are equal for all sub-images. Tests and simulations made with our correlation tracker have shown that such illumination changes from thin clouds can significantly degrade the accuracy of the position estimates from the cross-correlations unless compensated for. The importance of this normalization in AO however, is not equally obvious.

The timing for the AO system when run on an Athlon 1400 MHz system with fast DDR memory is shown in the same table. This is a simulation system reading saved images from disk and not doing any mirror control.

The time needed to process one full frame is 435  $\mu$ s on an Alpha 566 MHz and 422  $\mu$ s on an Athlon 1400 MHz. Already in September 2002, 2.6 GHz Athlon processors are available.<sup>10</sup> It is evident that both systems are capable of running the AO system. We conclude that inexpensive workstations quite clearly have the capacity to handle all aspects of the computations required by adaptive optics systems for low-latency (1–2 kHz frame rate) AO systems using 50 or more sub-apertures for night-time use and around 35 sub-apertures for use with solar telescopes.

## 2.7. Computational aspects

Crucial to the performance of an AO system is its closed-loop bandwidth. This bandwidth critically depends on the time delay of the AO system.<sup>11</sup> This time delay comes from the exposure of the CCD, the read-out time of the CCD and the computational delay. As illustrated in Ref. 11, the bandwidth of the AO system can drop from 25% to 5% of the sampling frequency when the read-out time of the CCD plus the time for computations is increased from zero to two frames, with 8% corresponding to the typical case of 1 frame delay. While using a CCD with higher frame rate will reduce the time delay, this is an expensive solution since in our case it would require a CCD that is not available commercially.

The 260  $\times$  260-pixel CCD used for our AO system is oversized. When used with 37 micro lenses, the required number of pixels is about 180  $\times$  200 pixels. By placing the sub-images optimally on the CCD chip, the read-out time is reduced by about 30% which gives an increase of the bandwidth by nearly 25%. Of even more importance is to arrange all computations such that processing of the sub-images is done on the fly. In the previous code, this was not done: The processing was done in two steps, first reading the image into memory and then subsequent processing. By using a reference image for cross-correlations from the current frame, computational delays were un-necessarily large. In the new code, a reference image is chosen from the previous frame allowing all processing on a sub-image to be done as soon as it is available in memory. This is checked by continuously monitoring how many lines have been DMA'd to system memory such that processing can start within micro-seconds after a given sub-image is in memory. This makes it possible to finish all computations within approximately 0.1 ms after reading the last sub-image.

Another possibility, which has not been implemented, for improving the bandwidth further is to reduce the exposure time of the CCD and control it such that the exposure is made immediately before the CCD is being read out. Our expectation, however, is that the bandwidth of the AO system will be adequate without this improvement.

## 2.8. Correlation Tracker

Bimorph mirrors can be used for excellent tip-tilt correction provided that the stroke is small. For larger stroke, unwanted higher-order aberrations are produced which degrade overall performance of the AO system. It was therefore decided to use a separate tip-tilt mirror. The upgraded correlation tracker runs a slightly modified version of the SVST software on a Compaq Alpha (500 MHz) system, tracking spots and small pores using a quad cell algorithm and on granulation using cross correlation.<sup>12</sup>

The cross correlation algorithm correlates a 64  $\times$  64 pixel reference image with a 48  $\times$  48 live image generating a 13  $\times$  13 “correlation” function (i.e. using  $\pm 6$  shift) in the same way as the AO system.

The bandwidth of the new CT has increased dramatically over the SVST system, primarily because a small 40 mm tip-tilt mirror with piezo actuators is used instead of the previous 200 mm mirror which was controlled by dc-motors. In addition, the CCD was upgraded from a Dalsa CA-D1 running at 800 Hz to a Dalstar CA-D6 CCD running at 955 Hz. The new tip-tilt mirror system uses 13 bit D/A converters kindly supplied by the Kiepenheuer Institute for Solar Physics.

## 3. OPTIMIZATION OF THE NEW 37-ELECTRODE MIRROR

In designing the new AO system, we optimized the bimorph mirror electrode geometry for best performance with the new Swedish solar telescope, using our optimized modal SH algorithm<sup>13</sup> with 37 hexagonal micro-lenses. The number of electrodes was varied from 35 to 40.

In this optimization, attention was paid also to the tail of high-order un-measurable modes that are produced by the mirror when applying voltages to produce low-order modes. In addition, the needed electrode voltages was balanced over the different electrodes such that saturation of the electrode voltages does not limit performance in good seeing.

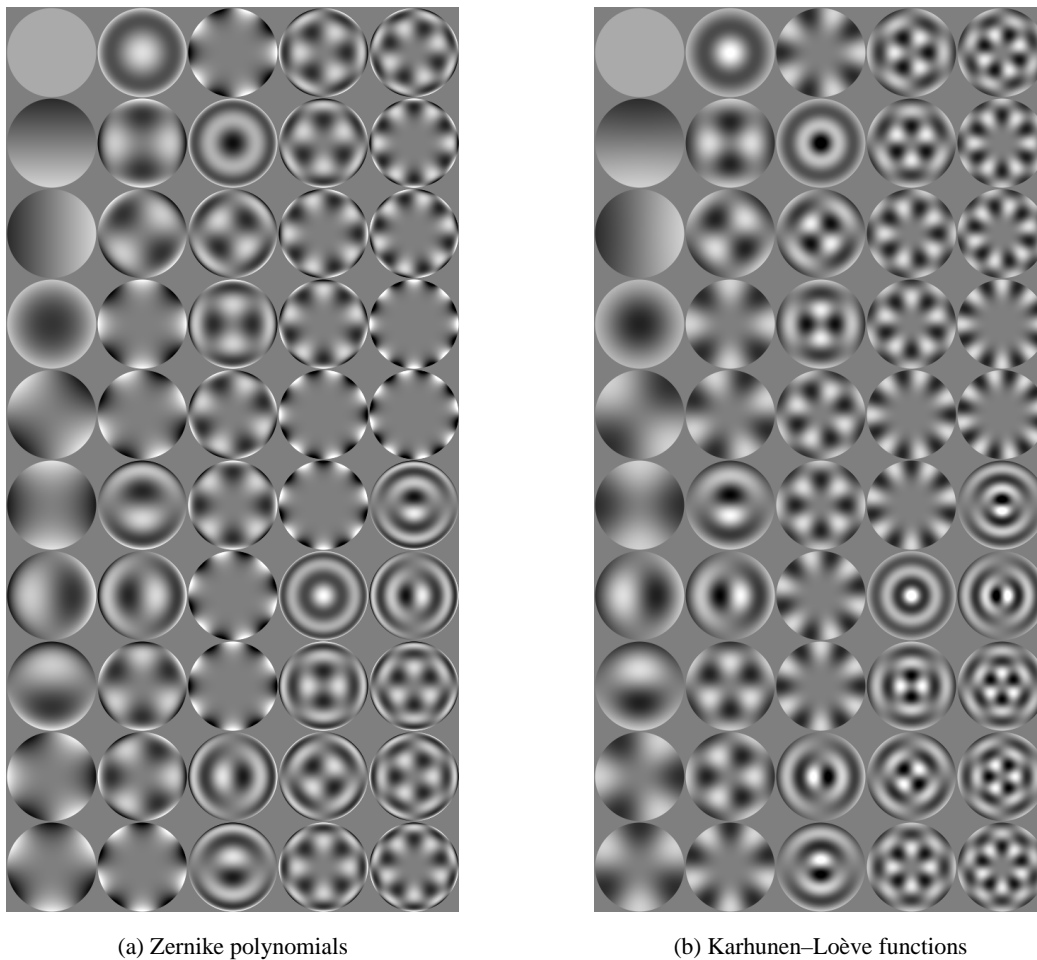


**Figure 3.** Comparison between the first 50 Zernike and Karhunen-Loève polynomials. The ordering follows Noll<sup>18</sup> and runs from top to bottom, left to right. Note that the Zernike polynomials in general show steeper gradients and more small-scale features near the edge of the pupil than is the case for KL polynomials. This difference gives a better match to turbulence induced seeing, bimorph mirrors and SH wavefront sensors for KL polynomials than for Zernikes.

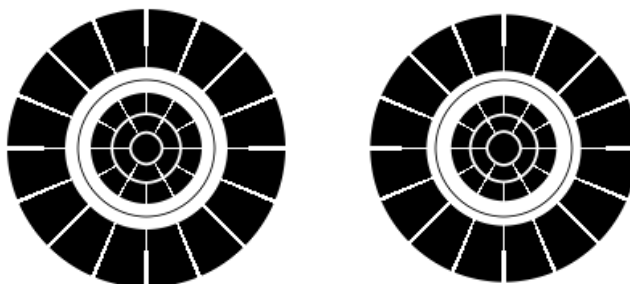
### 3.1. Atmospheric Karhunen-Loève functions

As pointed out earlier, KL functions are the optimal basis functions for compensating phase aberrations from atmospheric turbulence, a fact that follows from their diagonal covariance matrix, see e.g. Ref. 4. However, there are also reasons that have to do with how the sensor and the bimorph mirror work. As found in Refs. 14, 15 and confirmed by our simulations that KL functions are sensed much better than Zernikes by hexagonal SH sensors, due to the fact that the KL functions have smaller gradients close to the pupil perimeter and that structures close to the perimeter extend further into the pupil area (see Fig. 3). For the same reason, bimorph mirrors can more easily produce KL than Zernike modes. In the following we therefore restrict the analysis to KL functions, although we performed initial tests also with Zernike polynomials.

We constructed approximate KL functions as linear combinations of Zernike polynomials by diagonalizing the atmospheric covariance matrix, a procedure described in Ref. 16. We included Zernike modes up to Z 2000 in this procedure. We used the expression for the Zernike covariances given in Ref. 17. Our KL functions are numbered as the lowest included Zernike polynomials, according to the numbering scheme of Ref. 18 (see also Fig. 3).

Analysis of the SH sensor with 37 hex micro lenses indicates that it can well sense KL modes 2–36, 43–45, and 55.

Electrode ring	in/out	Orig.	Opt.
Center	o	0.212	0.242
Inner ring	i	0.253	0.285
	o	0.482	0.461
Middle ring	i	0.524	0.503
	o	0.812	0.782
Outer ring	i	1.188	1.192
	o	2.035	1.928



(a) Electrode radii/pupil radius

(b) Original

(c) Optimized

**Figure 4.** Result of a trial optimization of a 35-electrode bimorph mirror, labeled ESO35. The table compared the original electrode radii to those found by the optimization procedure described in the text. The electrode layouts, as used by the optimization procedure, is shown for the two configurations. This is not the geometry chosen for the new bimorph mirror.

### 3.2. Badness

A given mirror electrode geometry – as characterized by the inner and outer radii of the electrode rings, as well as the number and position of the electrodes within each ring – can be evaluated as follows.

We calculated the response for an electrode of each type (one in each ring of electrodes) from a thin plate model of the bimorph mirror. This is done by solving the Poisson equation where the RHS of the equation is unity within the electrode area and zero outside. This equation was solved numerically using Fourier transform techniques. The resulting mirror response is expanded in the phase mode basis set (up to  $M = 200$  modes). The responses of the other electrodes in the same ring were calculated by rotating the response of this electrode. The resulting “mirror response” matrix is then multiplied with the inverse of its largest square submatrix, with zeroed responses for unmeasurable modes. This gives a matrix, which describes the actual aberrations created by each of the controlled modes, i.e. the cross-talk matrix. We can then evaluate the residual variance in percent of what is expected from Kolmogorov statistics, taking into account also the “noise” of unwanted high-order aberrations.

The badness number is the variance of the residual wavefront weighted with atmospheric statistics for the KL modes, including also the variance of the unwanted high-order modes.

Note that for each mode, there is an optimum gain, which is less than unity, because turning up the gain to improve correction of this mode also increases the amplitudes of the high-order modes. The optimum gain for each mode is obtained to sub-pixel accuracy from the analysis and can be used to discriminate between well-corrected and badly corrected modes. In the optimization, modes with gain less than 0.7 were considered badly corrected and therefore switched off.

### 3.3. Mirror Electrode Optimization

Preliminary examination of badness space, i.e. how the badness number varies with respect to variations in the radii, indicated that the badness is a smooth function and that a global multi-dimensional optimization should work. In order to avoid unphysical electrode configurations, a large badness penalty (several orders of magnitude larger than the typical badness values) was given to configurations with a distance between rings or rings with widths smaller than 0.02% of the pupil radius. The resulting discontinuities made the problem less suited for ordinary, gradient-based optimizations algorithms. We therefore used the Downhill Simplex Method in Multidimensions.<sup>19</sup>

We start by trying to find an electrode geometry that can realize the measurable KL modes as well as possible, while producing as little as possible of un-measurable modes that will degrade performance directly and through aliasing (cross-talk). For the cases we tested, it converged to a function value tolerance of  $10^{-5}$  in  $\sim 10^2$  iterations. Generally we started the optimization from the radii of a design proposed earlier by Laplacian Optics and labeled ESO35, but also from the grid optima and in some cases from other configurations. In order to verify the optimization procedure, we re-optimized the radii of the ESO35 design. The results, shown in Fig. 4, agree quite well with the initially determined radii, derived from other criteria than used here.

### 3.4. Results

A more careful evaluation of promising electrode geometries was done with closed-loop simulations involving the SH sensor.

From theory, we calculated the wavefront gradients for each micro-lens and each KL. This gives a SH “response matrix”,  $\mathbf{X} = \mathbf{MK}$ , where  $\mathbf{X}$  are the 74 measured  $x, y$  sub-image positions from the 37 micro-lenses and  $\mathbf{M}$  is a  $74 \times M$  matrix. From  $\mathbf{M}$ , we extract a  $74 \times 45$  sub-matrix which has the elements corresponding to KL37–42 zeroed out. This sub-matrix is inverted by SVD to give  $\mathbf{K} = \mathbf{NX}$ . We then multiply  $\mathbf{M}$  with  $\mathbf{R}$  to get the slopes measured by the SH for each of the electrodes. Multiplication by  $\mathbf{N}$  gives the KL’s “measured” by the SH wavefront sensor *including* all the cross-talks from the mirror high-order aberrations. This corresponds to how we actually do our calibration of the present adaptive optics system.

Having obtained the final design of our mirror, we made additional experiments to improve it and noted the following: There are two main features that somewhat limit the performance. The first is the KL37 problem described below. The second problem is the geometry of the micro-lenses. The “default” geometry of 37 hexagonal micro-lenses has several micro-lenses too far away from the edge of the pupil. Simply moving 12 of the 18 lenses in the outer ring outwards, such that they are close to the edge of the pupil, improves performance.

A general problem is that the micro lens at the center of the pupil cannot sense the curvature of the center electrode. A bimorph mirror with a center electrode and three rings of electrodes surrounding it, can therefore produce higher even radial degrees of aberrations than the wavefront sensor can measure. Specifically, the mirror can produce 8th order spherical aberration, which in our labeling scheme corresponds to KL37. We have tried several electrode geometries that suppress KL37, but all these geometries gave unacceptable overall performance. We therefor decided to solve this problem by “adding” information from the bimorph model to the SH calibration such that KL37 can be identified and suppressed. This means that the control matrix is basically empirical, *but* that one row defining the voltages corresponding to KL37 is added to the empirical response matrix. Another way of doing this is to calibrate the mirror using “modes” of voltages corresponding to KLs as obtained from bimorph model and leave out the mode corresponding to KL37.

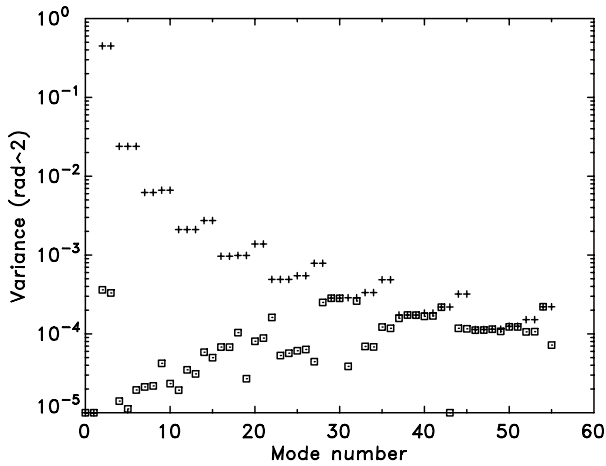
The geometry we finally chose is shown in Fig. 2. Note that the center electrode is fairly large. This was done in order to improve the “stroke”, as limited by the unwanted higher-order aberrations, of KL11 (spherical aberration), expected to be present from temperature gradients in the 1.1-m fused silica lens. This large center electrode has somewhat negative impact on higher-order coma terms KL 16 and 17 but this is marginal according to our calculations. We tried to improve also KL 22, higher order spherical aberration, but this made the center electrode even larger with negative effect on several aberrations with odd radial degree.

The best possible performance with this geometry is 1.26% residual variance when used with our hexagonal micro lens array.

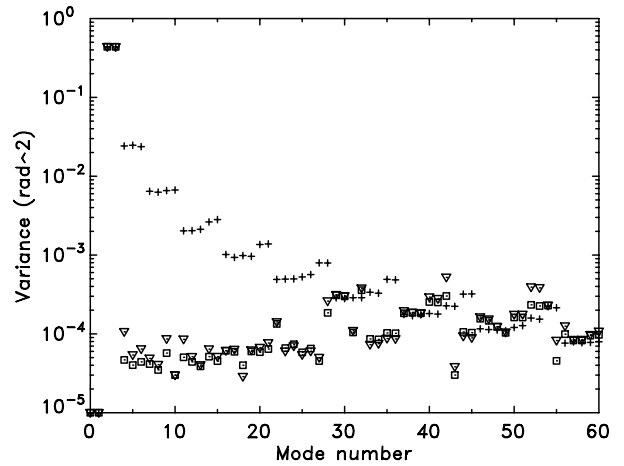
### 3.5. Predicted Performance

Figure 5(a) shows the best achievable performance as determined from the optimization procedure, corresponding to a residual variance of 1.26%. Note that nearly all KL modes up to KL28 are well corrected and that partial correction of several higher-order modes are possible. In Fig. 5(b) is shown a more realistic prediction of performance, based on closed-loop simulations. Note that the performance is somewhat better during the first iteration than during the last iteration, because in the first iteration, optimum gains were used, these gains were effectively set to unity at the last iteration. Note also that the wavefront variance for some higher-order modes is increased by correction of lower-order modes. The residual variance predicted from these simulations is 1.5%.

Finally, Fig. 6 shows histograms of the expected wavefront variance, based on the closed loop simulations. This histogram shows that a significant fraction of short-exposure images is expected to have a residual wavefront variance approaching 1.1% and very few should exceed 2%. This histogram is compared to a histogram predicting performance for the 50-cm SVST, without any adaptive optics. As can be seen, the performance should in all respects be better for the new 1-meter solar telescope when using the 37-electrode adaptive optics system than for the SVST without adaptive optics. Since the SVST frequently achieved near-diffraction limited image quality over extensive periods of time, it can be predicted with high degree of confidence that the new solar telescope should achieve this goal even more frequently even with the relatively simple AO system proposed here.



(a) Theoretical performance.



(b) Closed loop performance.

**Figure 5.** Predicted best possible performance from the optimization (a) and closed loop simulations (b) for the geometry of the new adaptive mirror. On the x-axis is labeled the KL-modes, following the ordering shown in Figure 3, on the y-axis the variances in radians squared, divided by  $(D/r_0)^{5/3}$  ( $D$  is the telescope diameter,  $r_0$  is the Fried parameter). The theoretical variances for turbulence induced seeing are indicated by +, the residual variances after correction by the AO system by  $\square$  for the first iteration and  $\nabla$  for the seventh iteration. Note the overshoot of some uncorrected higher-order aberrations.

### Acknowledgments

The wavefront sensor optics was designed and verified by Bo Lindberg, LensTech AB. The D/A converters of the tip-tilt mirror system was kindly supplied by the Kiepenheuer Institute for Solar Physics. The Swedish 1-m solar telescope is operated on the island of La Palma by the Royal Swedish Academy of Sciences in the Spanish Observatorio del Roque de los Muchachos of the Instituto de Astrofísica de Canarias.

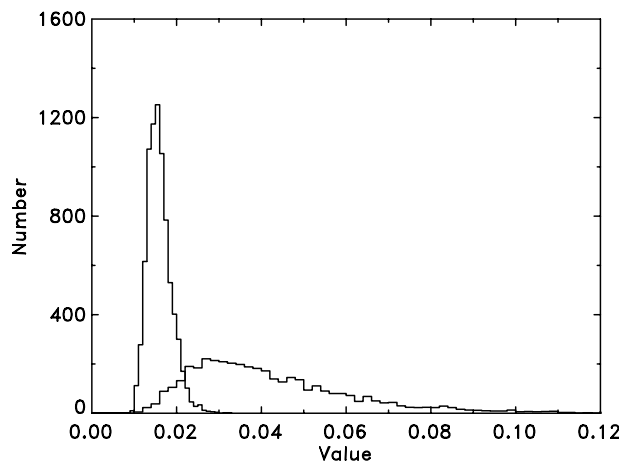


**Figure 6.** Histograms of expected wavefront variances for the new 1-m telescope with AO and old 50-cm telescope without AO under same seeing conditions. The leftmost peak is for the new telescope and the rightmost peak is for the old telescope.

## REFERENCES

1. AOptix Technologies, Inc. (formerly Laplacian Optics Inc.), 580 Division Street, Campbell, CA 95008, USA., 2002. <http://www.aoptix.com>.
2. G. B. Scharmer, M. Owner-Petersen, T. Korhonen, and A. Title, "The new Swedish solar telescope," in *High Resolution Solar Physics: Theory, Observations and Techniques*, T. Rimmele, R. R. Radick, and K. S. Balasubramaniam, eds., *Proc. 19th Sacramento Peak Summer Workshop, ASP Conf. Series vol. 183*, p. 157, 1999.
3. G. B. Scharmer, K. Bjelksjö, T. K. Korhonen, B. Lindberg, and B. Pettersson, "The new Swedish solar telescope," in *Innovative Telescopes and Instrumentation for Solar Astrophysics*, S. Keil and S. Avakyan, eds., *Proc. SPIE 4853-47*, 2002.
4. F. Roddier, "Theoretical aspects," in *Adaptive Optics in Astronomy*, F. Roddier, ed., ch. 3, pp. 25–56, Cambridge university press, Cambridge, UK, 1999.
5. Adaptive Optix Associates, Inc., Ten Wilson Road, Cambridge, MA 02138-1128, USA. <http://www.aoainc.com>.
6. R. A. Shine, L. Z. Porter, Z. Frank, J. B. Gurman, D. Pothier, and S. Ferguson, *A User's Guide to ANA*. Lockheed Palo Alto Research Laboratory, 1988.
7. M. Shand, G. B. Scharmer, and W. Wei, "Correlation tracking and adaptive optics control using off-the-shelf workstation technology," in *High Resolution Solar Physics: Theory, Observations and Techniques*, T. Rimmele, R. R. Radick, and K. S. Balasubramaniam, eds., *Proc. 19th Sacramento Peak Summer Workshop, ASP Conf. Series vol. 183*, p. 231, 1999.
8. G. B. Scharmer, M. Shand, M. G. Löfdahl, P. M. Dettori, and W. Wei, "A workstation based solar/stellar adaptive optics system," in *Adaptive Optical Systems Technologies*, P. L. Wizinowich, ed., *Proc. SPIE 4007*, pp. 239–250, 2000.
9. L. C. Stewart, A. C. Payne, and T. Levergood, "CRL technical report 92-10." <http://www.crl.research.digital.com/>, 1992.
10. Advanced Micro Devices, Inc., 2002. <http://www.amd.com>.
11. P.-Y. Madec, "Control techniques," in *Adaptive Optics in Astronomy*, F. Roddier, ed., ch. 6, pp. 131–154, Cambridge university press, Cambridge, UK, 1999.
12. M. Shand, W. Wei, and G. Scharmer, "3.8 ms latency correlation tracker for active mirror control based on a reconfigurable interface to a standard workstation," in *Field Programmable Gate Arrays (FPGAs) for Fast Board Development and Reconfigurable Computing*, J. Schewel, ed., *Proc. SPIE 2607*, pp. 145–154, 1995.
13. G. B. Scharmer and H. Blomberg, "Optimized Shack–Hartmann wavefront sensing for adaptive optics and post processing," in *High Resolution Solar Physics: Theory, Observations and Techniques*, T. Rimmele, R. R. Radick, and K. S. Balasubramaniam, eds., *Proc. 19th Sacramento Peak Summer Workshop, ASP Conf. Series vol. 183*, p. 239, 1999.
14. G.-m. Dai, *Theoretical studies and computer simulations of post-detection atmospheric turbulence compensation*. PhD thesis, Lund University, 1995.
15. M. E. Kasper, D. P. Looze, S. Hippler, M. Feldt, A. R. Weiß, A. Glindemann, and R. Davies, "A practical approach to modal basis selection and wavefront estimation," in *Adaptive Optical Systems Technologies*, P. L. Wizinowich, ed., *Proc. SPIE 4007*, pp. 592–599, 2000.
16. N. Roddier, "Atmospheric wavefront simulation using Zernike polynomials," *Optical Engineering* **29**(10), pp. 1174–1180, 1990.
17. G.-m. Dai, "Modal compensation of atmospheric turbulence with the use of Zernike polynomials and Karhunen–Loève functions," *Journal of the Optical Society of America A* **12**(10), pp. 2182–2193, 1995.
18. R. J. Noll, "Zernike polynomials and atmospheric turbulence," *Journal of the Optical Society of America* **66**(3), pp. 207–211, 1976.
19. W. H. Press, B. P. Flannery, S. A. Teukolsky, and W. T. Vetterling, *Numerical Recipes, The Art of Scientific Computing*, Cambridge University Press, 1986.